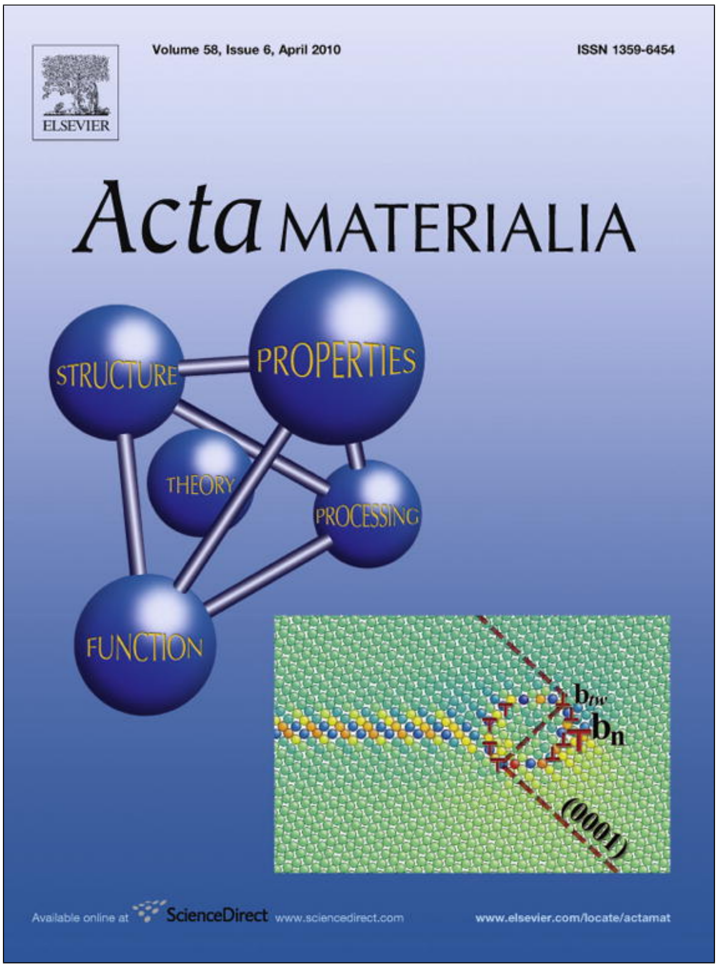
Volume 58, Issue 6, April 2010
ISSN 1359-6454
ELSEVIER
Acta MATERIALIA
STRUCTURE
PROPERTIES
THEORY
PROCESSING
FUNCTION
b_{tw}
b_n
(0001)
Available online at ScienceDirect www.sciencedirect.com
www.elsevier.com/locate/actamat

Available online at www.sciencedirect.com

ScienceDirect

Acta Materialia 58 (2010) 2155–2164

Acta MATERIALIA

www.elsevier.com/locate/actamat

A quantitative multi-phase field model of polycrystalline alloy solidification

Nana Ofori-Opoku *, Nikolas Provatas

McMaster University, Department of Materials Science and Engineering and Brockhouse Institute for Materials Research,
1280 Main Street West, Hamilton, Canada L8S-4L7

Received 29 September 2009; received in revised form 30 November 2009; accepted 1 December 2009
Available online 21 January 2010

Abstract

A multi-phase field model for quantitative simulations of polycrystalline solidification of binary alloys is introduced. During the free-growth stage of solidification, the model exploits the thin-interface analysis developed by Karma [3] in order to realistically capture bulk phase diffusion and the sharp interface corrections predicted by traditional models of solidification. During grain boundary coalescence, the model is constructed to reproduce the properties of repulsive grain boundaries described by Rappaz et al. [29]. The model provides a very simple mechanism for decoupling of solute and concentration fields at steady state, an important feature for calculating grain boundary energies.

Keywords: Solidification; Dendritic growth; Phase field modeling

1. Introduction

Phase field modeling is a robust methodology for examining complex microstructures in solidification and solid-state transformations. The approach is to minimize a generalized free energy functional written in terms of solute fields and order parameters—which are often reinterpreted as volume fractions. In the limit when the phase field interface goes to zero (the sharp-interface limit) these models can be shown to reduce to an appropriate Stefan-like problem, using sharp interface asymptotics techniques pioneered by Caginalp and co-workers [1–3]. Although mathematically rigorous, sharp-interface limits are impractical for numerical simulations in the limits of low solidification rates.

More recently, newer phase field models of solidification have been developed for binary alloys which offer several advantages, enabling more practical and quantitative simulations to be carried out in the so-called diffuse thin-interface limit—a limit where the physical dimensions of the interface can be many times larger than the capillary length, a feature crucial for practical numerical simulations of phase field models. An attractive feature of these models is that they are constructed in terms of free energy functionals that allow complete decoupling of diffusion and phase fields at steady state. This makes it possible to evaluate a simple relationship for the surface tension of an interface entirely in terms of the parameters of the steady-state phase field(s) [3–11].

A more important breakthrough in thin-interface modeling is the ability to cancel the effect of spurious kinetics and solute trapping caused by the use of interface widths that are large compared to the capillary length [3,7,12]. The main idea behind this important innovation is the use of the anti-trapping current that adjusts for solute imbalances—among other things—that would otherwise lead to solute trapping. This has made possible quantitative modeling in ideal [3,7] and non-ideal binary alloys [8,13], multi-component systems [11] and eutectic alloys [8]. It should be emphasized that while interface-induced kinetic

---

* Corresponding author. Tel.: +1 6479885072.
E-mail addresses: oforion@mcmaster.ca (N. Ofori-Opoku), provata@mcmaster.ca (N. Provatas).

1359-6454/$36.00 © 2009 Acta Materialia Inc. Published by Elsevier Ltd. All rights reserved.
doi:10.1016/j.actamat.2009.12.001

effects are relevant at high solidification rates, they are not relevant at low solidification rates when they are induced merely because the phase field interface is artificially expanded for numerical expediency.

It can be shown [14] that the advantages of simulating phase field models with diffuse interfaces is to reduce the time of simulation by a factor of $(d_o/W)^5$ in two dimensions. This efficiency is further enhanced significantly by simulating the phase field equations by adaptive mesh refinement [15–17]. This increases by many orders of magnitude the size of the physical domain that can be modeled, and slaves the simulation time to the interface arclength and not the physical domain. The combination of such multi-scale numerical methods and advanced asymptotic approaches has now made it possible to compare phase field simulations to metallurgically relevant systems and conditions [8,18,19].

The advances discussed above have been mostly applied to single-phase dendrite growth or directional solidification. There are also a significant number of so-called multi-phase field models of polycrystalline, multi-phase and multi-component solidification and solid-state transformations [20,21]. In many cases, solid-state phenomena are often diffusion controlled and thus do not suffer very much from spurious interface kinetics [5,6,22–25] of the type discussed above, even for moderately diffuse phase field interfaces. In the case of solidification, however, the spurious kinetic effects discussed above will plague all multi-phase models, for which a thin-interface limit is presently not available [26]. A similar comment can be made about polycrystalline solidification models utilizing an orientational order parameter. Exceptions to this general trend include the work of Folch et al. who have developed a specific phase field model to simulate triple junctions using diffuse interfaces [8], and the the work of Steinbach [27] who has recently proposed using Kim's anti-trapping formalism [11] in his multi-phase field approach—although the convergence properties of this proposed approach have not been demonstrated.

There is a class of solidification phenomena of industrial importance that requires quantitative modeling of the entire solidification path, from free dendritic growth to grain boundary impingement and back-diffusion in the solid state. There are presently few quantitative multi-phase field solidification models suitable for an arbitrary number of crystal orientations and which contain a demonstrated thin-interface limit. This paper reports the details of a new multi-phase field model developed in Ref. [28]. The model extends the anti-trapping formalism of Refs. [3,7] to a multi-phase field model in order to be able to quantitatively simulate solidification, grain impingement and solid-state diffusion in multiply oriented crystals in a binary alloy. The steady-state and kinetic properties of free solid–liquid interfaces are first demonstrated. The model's grain boundary coalescence properties are then benchmarked against the work of Rappaz et al. [29]. Finally, the grain boundary energy of the model is characterized.

2. Dilute binary alloy model with multiple order parameters

The starting point is the free energy of an ideal, dilute binary alloy of species A and B, containing N grains, each being of the same phase but of varying crystal orientation. Each grain i $(1 \leqslant i \leqslant N)$ is defined in terms of an order parameter ϕ_i, each of which varies from $0 < \phi_i < 1$, where 0 represents the liquid and $\phi_i = 1$ represents solid. The free energy will be constructed so that different order parameters cannot completely overlap, so that in the bulk of each grain, $\phi_i = 1$, and all other $\phi_j = 0$ (for $j \neq i$). At any point in space, the system can be represented in a multi-dimensional phase space by a state vector $\vec{\phi} \equiv (\phi_1, \phi_2, \phi_3, \cdots, \phi_N)$. In this formalism, the liquid is defined by $\vec{\phi} = \mathbf{0}$, while the bulk of grain i is defined by the phase space vector $\vec{\phi} = \hat{e}_i \equiv (0, 0, 0, \cdots \phi_i = 1, \cdots, 0, 0, 0)$. The vector $\hat{e}_i$ represents one of the unit vectors of this multi-dimensional phase space defined by the order parameters. Regions in space where two or more grains i, j, k, etc., overlap are defined by the vector $\vec{\phi} \equiv (0 \cdots \phi_i, \cdots \phi_j, \cdots, \phi_k, \cdots)$, where $0 < \phi_i, \phi_j, \phi_k < 1$. For consistency, the parameters of the model must in principle be chosen such that order parameters always satisfy $0 \leqslant \phi_i + \phi_j + \phi_k + \cdots \leqslant 1$. This will not prove to be a stringent condition.

2.1. Free energy

The free energy of this system is given by:

$$F(c, \vec{\phi}, T) = \int d\mathbf{r} \left\{ \sum_{i=1}^{N} \frac{1}{2} |\epsilon(\vec{\phi}) \nabla \phi_i|^2 + f(\vec{\phi}, c, T) + f_{\text{int}}(\vec{\phi}) \right\} \tag{1}$$

where $\epsilon(\vec{\phi})$ is an anisotropic gradient energy coefficient between any solid phase and liquid or between solid i and solid $j(\neq i)$. The bulk free energy density $f(\vec{\phi}, c, T)$ is expanded to lowest order in c and T and to fourth order in ϕ_i, yielding:

$$f(\vec{\phi}, c, T) = H f_D(\vec{\phi}) + \frac{RT_m}{v_o}[c \ln c - c] + f^A(T_m) - \Delta T \left[s_L - \frac{L}{T_m} \tilde{g}(\vec{\phi}) \right] + [\epsilon_L + \Delta\epsilon \bar{g}(\vec{\phi})]c \tag{2}$$

where $f_D(\vec{\phi}) = \sum_i \phi_i^2 (1 - \phi_i)^2$ is a double-well potential barrier between pure solid and pure liquid, for all i, and H is the energy barrier between solid and liquid. The function $f_{\text{int}}(\vec{\phi})$ defines the interaction energy between grain i and all other grains $j(\neq i)$. In this work the interaction energy of the form:

$$f_{\text{int}}(\vec{\phi}) = \sum_i \sum_{j>i} \alpha \phi_i^2 \phi_j^2 \tag{3}$$

[30,31] is used, where α is a constant.

Other functions and constants in Eq. (2) are as follows. The constant $f^A(T_m)$ is the free energy of pure A evaluated at its melting temperature T_m, $\Delta T = T - T_m$, R is the natural gas constant and v_o is the molar volume of the solid.

The parameter s_L is the entropy of the liquid, $\epsilon_L(\epsilon_s)$ is the internal energy of the liquid(solid), $\Delta\epsilon = \epsilon_s - \epsilon_L$ and L is the latent heat of fusion. The scalar function $\tilde{g}(\vec{\phi})$ interpolates entropy between solid ($\vec{\phi} = \hat{e}_i$) and liquid ($\vec{\phi} = \mathbf{0}$), while $\bar{g}(\vec{\phi})$ similarly interpolates the internal energy.

The chemical part of the bulk free energy in Eq. (2) (denoted hereafter as f_c) can be obtained by a two-step process. Following Kim [4], $f_c = f_s\tilde{g}(\vec{\phi}) + (1 - \tilde{g}(\vec{\phi}))f_L$, where f_L and f_s are the free energy densities of the liquid and solid alloy phases. This leads to a bulk free energy of a binary alloy in which the entropy and internal energy are both interpolated by $\tilde{g}(\vec{\phi})$. In order to be able to decouple the phase field and concentration at steady state, the method of Ref. [7] is then used, in which different interpolation functions are introduced for the entropy density ($\tilde{g}(\vec{\phi})$) and for the internal energy density ($\bar{g}(\vec{\phi})$), leading to Eq. (2).

The form of the interpolation function $\tilde{g}(\phi)$ is constructed to satisfy $\tilde{g}(\vec{\phi} = \mathbf{0}) = 0, \tilde{g}(\vec{\phi} = \hat{e}_i) = 1$ and $0 < \tilde{g}(\vec{\phi}) < 1$ for a general $\vec{\phi}$. The function $\bar{g}(\vec{\phi})$ has the same limits as $\tilde{g}(\vec{\phi})$ and is "slaved" to the form:

$$\bar{g}(\vec{\phi}) = \frac{1}{\ln k}\ln[1 - (1-k)\tilde{g}(\vec{\phi})] \tag{4}$$

where k is the partition coefficient of the dilute binary alloy, which defines the ratio of equilibrium solid to liquid concentrations. Following Ref. [32], in this work $\tilde{g}(\vec{\phi}) = \sum_i G(\phi_i)$, where $G(0) = 0, G(1) = 1$, while the derivatives with respect to ϕ_i satisfy $G'(0) = G'(1) = 0$. The specific algebraic form of $G(\phi_i)$ used here is $G(\phi_i) = \phi_i^3(6\phi_i^2 - 15\phi_i + 10)$.

2.2. Phase coexistence

It is instructive to analyze the mean field properties of the bulk terms of the free energy of Eq. (2), starting first with the calculation of the equilibrium phase diagram of this alloy. The generalized chemical potential is given by:

$$\mu \equiv \frac{\partial f(\vec{\phi}, c)}{\partial c} = \frac{RT_m}{v_o}\ln c + \epsilon_L + \Delta\epsilon\bar{g}(\vec{\phi}) \tag{5}$$

Assuming equilibrium and evaluating $\mu = \mu_{\mathrm{eq}}$ in a bulk solid i ($\vec{\phi}_o = \hat{e}_i$) and in the bulk liquid ($\vec{\phi}_o = \mathbf{0}$), respectively, gives

$$\mu_s^{\mathrm{eq}} = \frac{RT_m}{v_o}\ln c_s + \Delta\epsilon + \epsilon_L$$
$$\mu_L^{\mathrm{eq}} = \frac{RT_m}{v_o}\ln c_L + \epsilon_L \tag{6}$$

where c_s and c_L represent equilibrium solid and liquid concentrations at temperature T, and $\vec{\phi}_o$ tracks the equilibrium phase field profile between some grain i and the liquid. Setting $\mu_s^{\mathrm{eq}} = \mu_L^{\mathrm{eq}} \equiv \mu_{\mathrm{eq}}$ gives the partition coefficient, i.e.

$$k \equiv \frac{c_s}{c_L} = \exp\left(-\frac{v_o\Delta\epsilon}{RT_m}\right) \tag{7}$$

It will be useful in what follows to invert Eq. (7), obtaining $\Delta\epsilon v_o/RT_m = -\ln k$.

Solving $\mu_{\mathrm{eq}} = \mu_s^{\mathrm{eq}}$ and $\mu_{\mathrm{eq}} = \mu_L^{\mathrm{eq}}$, along with the equation $f(c_s, \vec{\phi}_o = \hat{e}_i) - f(c_L, \vec{\phi}_o = \mathbf{0}) = \mu_{\mathrm{eq}}(c_L - c_s)$, gives μ_{eq} and the liquidus line of a dilute ideal binary alloy:

$$T = T_m - \left[\frac{RT_m^2(1-k)}{Lv_o}\right]c_l \tag{8}$$

where the liquidus slope is defined by:

$$m_L = -\frac{RT_m^2(1-k)^2}{Lv_o} \tag{9}$$

2.3. Steady-state interface profiles

2.3.1. Concentration

The steady-state concentration profile across a planar interface is found by considering the chemical potential μ_{eq} at a given temperature. This is a constant given by:

$$\mu_{\mathrm{eq}} = \frac{RT_m}{v_o}\ln c_o(\mathbf{r}) + \epsilon_L + \Delta\epsilon\bar{g}(\vec{\phi}_o(\mathbf{r})) \tag{10}$$

where $c_o(\mathbf{r})$ is the steady-state concentration field across the interface between one or more grains and $\vec{\phi}_o(\mathbf{r})$ is the vector of steady-state phase fields. For example, a single solid–liquid interface across some grain i is described by $\vec{\phi}_o = (0,0,0,\cdots,\phi_i^o(\mathbf{r}),\cdots,0,0,0)$. More generally, the steady-state phase field vector for two overlapping grains is represented by $\vec{\phi}_o = (0,0,0,\cdots,\phi_i^o(\mathbf{r}),\cdots,0,0,0,\cdots,\phi_j^o(\mathbf{r}),\cdots,0,0,0)$, where i and j represent the phase field profiles of adjacent grains. Solving for $c_o(\mathbf{r})$ and using the second of Eq. (6) to eliminate $\epsilon_L - \mu_{\mathrm{eq}}$ gives:

$$\frac{c_o(\mathbf{r})}{c_o^l} \equiv \frac{c_o(\vec{\phi}_o(\mathbf{r}))}{c_o^l} = \exp[\ln k\bar{g}(\vec{\phi}_o)] \tag{11}$$

where c_o^l is used as a reference liquid concentration at a given quench temperature. Eq. (11) is the same form used in Ref. [7] for the steady-state concentration profile across a solid–liquid interface in a dilute binary alloy. Using Eq. (4), the steady-state concentration can also be written as:

$$\frac{c_o(\vec{\phi}_o(\mathbf{r}))}{c_o^l} = [1 - (1-k)\tilde{g}(\vec{\phi}_o)] \tag{12}$$

It will be shown below that the form of Eq. (12) also describes the steady-state concentration across a solid–solid interface.

2.3.2. Phase fields

The equilibrium phase field profile across a planar solid–liquid interface, $\vec{\phi}_o = (0,0,0,\cdots,\phi_i^o(\mathbf{r}),\cdots,0,0,0)$, is given by solving the Euler–Lagrange equation $\delta F/\delta\phi_i = 0$ in one dimension:

$$W_o^2\frac{d^2\phi_i^o}{dx^2} - \frac{\partial f_D(\phi_i^o)}{\partial\phi_i^o} - \frac{\partial f_{\mathrm{int}}(\vec{\phi}_o)}{\partial\phi_i^o} + \left[-\frac{\Delta TL}{T_m}\frac{\partial\tilde{g}(\vec{\phi}_o)}{\partial\phi_i^o} - \Delta\epsilon\frac{\partial\bar{g}(\vec{\phi}_o)}{\partial\phi_i^o}c_o(\vec{\phi}_o(\mathbf{r}))\right] = 0 \tag{13}$$

with $W_o = \epsilon_o/\sqrt{H}$, where ϵ_o is the coefficient $\epsilon(\vec{\phi})$ evaluated for the case of an isotropic solid–liquid interface. The large bracketed term in Eq. (13) is made to vanish by the choice of interpolation functions. This implies that each order parameter equation decouples entirely from the concentration in the steady state. This will make it possible to compute the solid–liquid or solid–solid surface energies only in terms of phase field parameters.

For example, in the case of an isolated solid–liquid interface corresponding to grain i, the interaction term $f_{\text{int}} = 0$ and decoupling of order parameter and concentration, fixes the lowest-order phase field solution across the solid–liquid interface to the simple hyperbolic tangent profile, $\phi_i^o(x) = \left[1 - \tanh(x/\sqrt{2}W_o)\right]/2$, where x denotes the direction normal to the interface. This fixes the model's liquid–solid surface energy to be:

$$\gamma_{sl} = \frac{2\sqrt{2}}{3} W_o H \tag{14}$$

3. Dynamics

3.1. Variational formulation

The equations of motion for the fields are given by the standard variational minimization of the free energy:

$$\begin{aligned}\tau(\vec{\phi})\frac{\partial \phi_i}{\partial t} = {} & \nabla \cdot (W^2(\vec{\phi})\nabla\phi_i) - \partial_x\left(W(\vec{\phi})\frac{\partial W}{\partial \vec{\phi}}\frac{\partial \vec{\phi}}{\partial y}\right) \\ & + \partial_y\left(W(\vec{\phi})\frac{\partial W}{\partial \vec{\phi}}\frac{\partial \vec{\phi}}{\partial x}\right) - \frac{df_D}{d\phi_i} - \frac{1}{H}\frac{\partial f_c}{\partial \phi_i} - \frac{1}{H}\frac{\partial f_{\text{int}}}{\partial \phi_i}\end{aligned} \tag{15}$$

$$\frac{\partial c}{\partial t} = \nabla \cdot (M(c, \vec{\phi})\nabla\mu) \tag{16}$$

where $\mu = \delta F/\delta c$ is given by Eq. (5), and the constant $\tau(\vec{\phi}) = 1/(K_\phi(\vec{\phi})H)$, where K_ϕ is an anisotropic phase field mobility (assumed here the same for all ϕ_i) and $W(\vec{\phi}) \equiv \epsilon(\vec{\phi})/\sqrt{H} = W_o a_s(\vec{\phi})$ is an effective anisotropic gradient coefficient, which depends on the type of interfaces being considered (W_o is a characteristic interface width). The function f_c has been defined to denote the chemical portion of the free energy f. For dilute binary alloys the mobility M is set to $M(c, \vec{\phi}) = (D_L v_o/RT_m)q(\vec{\phi})c$. where $q(\vec{\phi})$ interpolates the diffusion from its liquid-phase value D_L, when $q(\vec{\phi} = 0) = 1$, to its solid-state value D_s, which implies that $q(\vec{\phi} = \hat{e}_i) = \xi$, where $\xi = D_s/D_L$.

The driving force $\partial f_c(\vec{\phi}, c, T)/\partial\phi_i$ in Eq. (15) can be simplified via Eqs. (4) and (12) analogously to the single-order parameter case shown in Ref. [7]. Specifically,

$$\frac{\partial f_c(\vec{\phi}, c, T)}{\partial \phi_i} = -\frac{RT_m \ln k}{v_o}\frac{\Delta T}{m_L c_o^l}(c(\vec{x}) - c_o(\vec{\phi}))\bar{g}'(\vec{\phi}) \tag{17}$$

Eq. (17) can be further simplified by eliminating $c(\vec{x})$ by considering a dimensionless chemical potential:

$$u = \frac{v_o}{RT_m}(\mu - \mu_E) = \ln\left(\frac{c}{c_o^l[1 - (1-k)\tilde{g}(\vec{\phi})]}\right) \tag{18}$$

where μ_E is the reference equilibrium chemical potential of the liquid. Eqs. (18) and (12) are used to write:

$$\left(\frac{c(\vec{x})}{c_o^l} - \frac{c_o(\vec{\phi})}{c_o^l}\right)\bar{g}'(\vec{\phi}) = -\frac{(1-k)}{\ln k}(e^u - 1)\tilde{g}'(\vec{\phi}) \tag{19}$$

where $\bar{g}$ has been eliminated in favour of $\tilde{g}$ using Eq. (4). Eqs. (17) and (19) finally give:

$$\frac{1}{H}\frac{\partial f_c(\vec{\phi}, c, T)}{\partial \phi_i} = \lambda\frac{(e^u - 1)}{1-k}\tilde{g}'(\vec{\phi}) \tag{20}$$

where $\tilde{g}'(\vec{\phi})$ represents $G'(\phi_i)$, and the coupling constant λ is defined by:

$$\lambda \equiv \frac{RT_m(1-k)^2 c_o^l}{v_o H} \tag{21}$$

Eq. (20) can be used to rewrite the phase field equation as:

$$\begin{aligned}\tau(\vec{\phi}, T)\frac{\partial \phi_i}{\partial t} = {} & \nabla \cdot (W^2(\vec{\phi})\nabla\phi_i) - \partial_x\left(W(\vec{\phi})\frac{\partial W}{\partial \vec{\phi}}\frac{\partial \vec{\phi}}{\partial y}\right) \\ & + \partial_y\left(W(\vec{\phi})\frac{\partial W}{\partial \vec{\phi}}\frac{\partial \vec{\phi}}{\partial x}\right) - \phi_i^2(1-\phi_i)^2 \\ & - \omega\phi_i\sum_{j>i}\phi_j^2 - \frac{\lambda(T)}{(1-k(T))}(e^u - 1)\tilde{g}'(\phi_i)\end{aligned} \tag{22}$$

where $\omega = \alpha/H$. The coefficients τ, λ and the partition coefficient k have been made temperature dependent to demonstrate the ability to handle a general binary alloy with nonlinear phase coexistence boundaries, as described in Ref. [13].

For uniform continuous cooling, a more convenient reference concentration is c_∞, the average alloy composition. This modifies Eq. (18) to:

$$u = \frac{v_o}{RT_m}(\mu - \mu_\infty) = \ln\left(\frac{c}{c_\infty[1 - (1-k)\tilde{g}(\vec{\phi})]}\right) \tag{23}$$

making it possible to rewrite

$$\left(\frac{c(\vec{x})}{c_o^l} - \frac{c_o(\vec{\phi})}{c_o^l}\right)\bar{g}'(\vec{\phi}) = -\frac{c_\infty}{c_o^l}\left(e^u - \frac{c_o^l}{c_\infty}\right)\frac{(1-k)}{\ln k}\tilde{g}'(\vec{\phi}) \tag{24}$$

where, using Eq. (4), $\bar{g}$ has been eliminated in favour of $\tilde{g}$. Following similar algebraic steps that lead to Eq. (20), the driving term can be recast as:

$$\frac{1}{H}\frac{\partial f_c(\vec{\phi}, c, T)}{\partial \phi_i} = \lambda\frac{(e^u - \frac{c_o^l}{c_\infty})}{1-k}\tilde{g}'(\vec{\phi}) \tag{25}$$

where now the coupling constant becomes:

$$\lambda = \frac{RT_m(1-k)^2 c_\infty}{v_o H} \tag{26}$$

For a dilute ideal alloy it is straightforward to write:

$$\left(e^u - \frac{c_o^l}{c_\infty}\right) = e^u - 1 - \frac{T - T_L}{m_L c_\infty} \tag{27}$$

The order parameter equation of motion for uniform cooling thus becomes:

$$\begin{aligned}\tau(\vec{\phi})\frac{\partial\phi_i}{\partial t} &= \nabla\cdot(W^2(\vec{\phi})\nabla\phi_i) - \partial_x\left(W(\vec{\phi})\frac{\partial W}{\partial\vec{\phi}}\frac{\partial\vec{\phi}}{\partial y}\right)\\ &\quad + \partial_y\left(W(\vec{\phi})\frac{\partial W}{\partial\vec{\phi}}\frac{\partial\vec{\phi}}{\partial x}\right) - \phi_i^2(1-\phi_i)^2\\ &\quad - \omega\phi_i\sum_{j>i}\phi_j^2 - \frac{\lambda}{(1-k)}\left(e^u - 1 - \frac{T-T_L}{m_L c_\infty}\right)\tilde{g}'(\phi_i)\end{aligned} \tag{28}$$

3.2. Nonvariational formulation

To eliminate spurious kinetics inherent in all binary alloy phase field models employing diffuse interfaces, the approaches of Karma and co-workers are employed [3,7,8]. First, the interpolation function $\tilde{g}(\vec{\phi})$ entering the dimensionless chemical potential u is replaced by a new interpolation function $h(\vec{\phi})$, which has the same limits as $\tilde{g}(\vec{\phi})$. In particular, the original function u in the chemical potential is replaced by:

$$u = \frac{v_o}{RT_m}(\mu - \mu_E) = \ln\left(\frac{c}{c_o^l[1-(1-k)h(\vec{\phi})]}\right) \tag{29}$$

while the u for uniform cooling yields:

$$u = \frac{v_o}{RT_m}(\mu - \mu_\infty) = \ln\left(\frac{c}{c_\infty[1-(1-k)h(\vec{\phi})]}\right) \tag{30}$$

These new definitions do not affect the equilibrium results; however, the definition for the equilibrium concentration profile, Eq. (12), needs modification as $h(\vec{\phi})$ replaces $\tilde{g}(\vec{\phi})$, resulting in:

$$\frac{c_o(\vec{\phi}_o(\mathbf{r}))}{c_o^l} = [1-(1-k)h(\vec{\phi}_o)] \tag{31}$$

In this work, the simple choice $h(\vec{\phi}) = \sum_i \phi_i$ is employed. This follows the usual summation rule of order parameters in the chemical potential.

The second change to the variational model is a modified diffusion equation, Eq. (16), that employs a so-called anti-trapping flux term. In this multi-phase field approach, this source is a sum of currents arising from each order parameter. This is given by:

$$\vec{j}_{\text{at}} = -a_t W_o \chi(1-k)e^u \sum_i \frac{\partial\phi_i}{\partial t}\frac{\nabla\phi_i}{|\nabla\phi_i|} \tag{32}$$

where $\chi = c_l^o$ is used for isothermal quenches into the coexistence region, and $\chi = c_\infty$ for the model with uniform cooling. It is noted that during free dendritic growth, only one current in Eq. (32) will be active at any point in space as defined by the multi-dimensional phase space vector $\vec{\phi}$. Therefore, the evaluation of the sum at any point in space (where an interface is in motion), only yields a value corresponding to the single-order parameter that exists. Upon merger, where all $\partial_t\phi_i$ tend to zero, the current $\vec{j}_{\text{at}}$ essentially vanishes.

The interpolation function $h(\vec{\phi})$, the anti-trapping flux and the diffusivity function $q(\vec{\phi})$ provide three degrees of freedom with which it has been shown that all spurious effects occurring at moving solid–liquid interfaces can be eliminated to second order. Here, the diffusion interpolation function is chosen to be of the form $q(\vec{\phi}) = \left(1 - \sum_i\phi_i\right)/[1-(1-k)h(\vec{\phi})] + \xi\sum_i\phi_i$. The combined equations of motion for the nonvariational fomulation now become:

$$\begin{aligned}\tau(\vec{\phi})\frac{\partial\phi_i}{\partial t} &= \nabla\cdot(W^2(\vec{\phi})\nabla\phi_i) - \partial_x\left(W(\vec{\phi})\frac{\partial W}{\partial\vec{\phi}}\frac{\partial\vec{\phi}}{\partial y}\right)\\ &\quad + \partial_y\left(W(\vec{\phi})\frac{\partial W}{\partial\vec{\phi}}\frac{\partial\vec{\phi}}{\partial x}\right) - \phi_i^2(1-\phi_i)^2\\ &\quad - \omega\phi_i\sum_{j>i}\phi_j^2 - \frac{\lambda}{(1-k)}(e^u - 1)\tilde{g}'(\phi_i)\end{aligned} \tag{33}$$

$$\frac{\partial c}{\partial t} = \nabla\cdot(D_L q(\vec{\phi})c\nabla u - \vec{j}_{\text{at}}) \tag{34}$$

where Eq. (29) is used for u. For uniform cooling, the phase field equations are modified to:

$$\begin{aligned}\tau(\vec{\phi})\frac{\partial\phi_i}{\partial t} &= \nabla\cdot(W^2(\vec{\phi})\nabla\phi_i) - \partial_x\left(W(\vec{\phi})\frac{\partial W}{\partial\vec{\phi}}\frac{\partial\vec{\phi}}{\partial y}\right)\\ &\quad + \partial_y\left(W(\vec{\phi})\frac{\partial W}{\partial\vec{\phi}}\frac{\partial\vec{\phi}}{\partial x}\right) - \phi_i^2(1-\phi_i)^2\\ &\quad - \omega\phi_i\sum_{j>i}\phi_j^2 - \frac{\lambda}{(1-k)}\left(e^u - 1 - \frac{T-T_L}{m_L c_\infty}\right)\tilde{g}'(\phi_i)\end{aligned} \tag{35}$$

$$\frac{\partial c}{\partial t} = \nabla\cdot(D_L q(\vec{\phi})c\nabla u - \vec{j}_{\text{at}}) \tag{36}$$

where Eq. (30) is now used for u.

4. Free dendritic growth

A crucial property of the present multi-order parameter model is that it exhibits the correct solute segregation and re-distribution during solidification of free growing dendrites. The convergence of the model was studied by conducting two-dimensional simulations of two isothermal free dendrites, grown using Eqs. (33) and (34). The anisotropy was chosen to have the standard fourfold form $W(\psi) = W_o a_s(\psi)$, where $a_s(\psi) = 1 + \epsilon_4\cos 4\psi$ and ψ is the angle of the interface normal of each grain with the x-axis. The timescale $\tau(\psi) = \tau_o a_s(\psi)^2$ and $\lambda = D_L\tau_o/a_2W_o^2$, making the kinetic coefficient term β negligible [3,7] (τ_o is a characteristic time and $a_2 = 0.8839$ [3]). Eqs. (33) and (34) were simulated in a dimensionless form using a finite-difference Euler time-stepping method. The other phase field model parameters used are listed in Table 1. The initial condition comprised two circular seeds of radius $r = 22d_o$, each at an orientation of 45° with respect to the x-axis, and $u = \ln[1 - (1 - k)\Omega]$, where the supersaturation $\Omega = (c_L - c_\infty)/(c_L - c_s)$ with c initially defined by Eq. (29).

Fig. 1 plots the scaled dimensionless dendrite tip velocity vs. time. Convergence of the model implies that, for different interface widths (W_o), the dimensionless steady-state dendrite tip speed of each crystal must collapse to the same solution. This is indeed the case as seen from Fig. 1. Fig. 2 plots the center line solute concentration profiles along the dendrites corresponding to Fig. 1. Once again, there is excellent convergence for each W_o/d_o in each crystal, and the solid-state solute impurity level is precisely as predicted by the equilibrium phase diagram, appropriately corrected for by the Gibbs–Thomson curvature correction.

The onset of grain boundary coalescence begins when dendrite tips begin to interact. It is noted that at this stage interface motion becomes predominantly curvature and diffusion controlled, rendering the anti-trapping term essentially unnecessary. This is automatically taken care of by the construction of the anti-trapping current $\vec{j}_{at}$, since it scales with $\partial_t \phi$, which is observed to rapidly tend to zero as grain impingement sets in.

Table 1
Parameters for free growth.

Parameter	Value
ϵ_4	0.02
k	0.15
Δx	0.4
Δt	0.008
Ω	0.55
a_t	$1/(2\sqrt{2})$

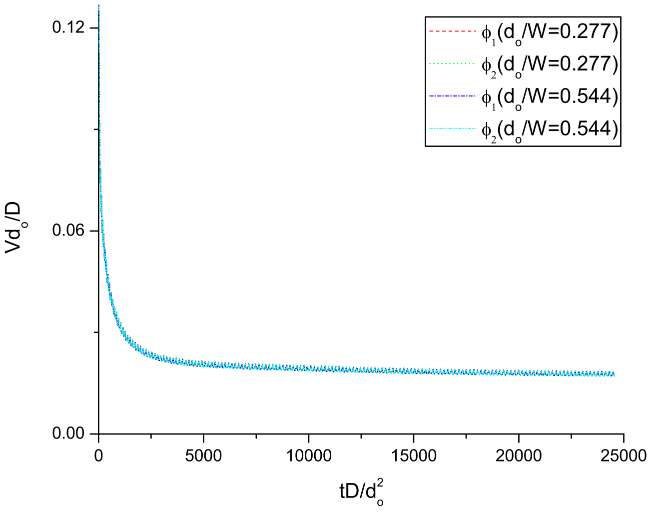

Fig. 1. Scaled dendrite tip velocity vs. scaled time for two different ratios of d_o/W_o, with parameters from Table 1.

5. Grain boundaries

This section examines the steady-state properties of grain boundaries at coalescence and the grain boundary energies that can be predicted by the present model.

5.1. Steady-state interface concentration

Below the solidus, equilibrium theory predicts a single phase. In practice, there is a single phase with multiple (meta-stable) grain boundaries. Without back-diffusion in the solid (i.e. solid state diffusion) the boundaries remain wet at temperatures well below the solidus [29]. When back-diffusion is considered, it is expected that the thermodynamic driving force required to homogenize the bulk phases to the average concentration (c_∞) will tend to drive excess solute out of a grain boundary and allow the grains to merge. This driving force is achieved via diffusion of the excess solute piled up in the last liquid film from the boundary into the surrounding solid. In the ideal case of equilibrium with no adsorption at a grain boundary, $c_o(\vec{\phi}_o) = c_\infty$, everywhere and the phase fields corresponding to two impinged grains i and j should in theory sum to 1 (totally ordered grain boundary), i.e. $\phi_i + \phi_j = 1$. In this case Eq. (30) gives:

$$c_o(\vec{\phi}_o) = c_\infty e^u[1 - (1 - k)h(1)] = c_\infty \Rightarrow e^u = \frac{1}{k} \tag{37}$$

Most grain boundaries exhibit some segregation (adsorption) and there is only partial order at the grain boundary, modeled here as an overlap between corresponding order parameters across the grain boundary, i.e. $\phi_i + \phi_j < 1$. Physically, a grain boundary can be crudely thought of as an amorphous undercooled solid [33]. In this case solute segregation is still modeled via Eq. (30), but e^u must be computed by numerically determining (for a given interaction ω) the crossing $\phi_i + \phi_j$ and the maximum concentration c_{max} in the middle of the grain boundary. In

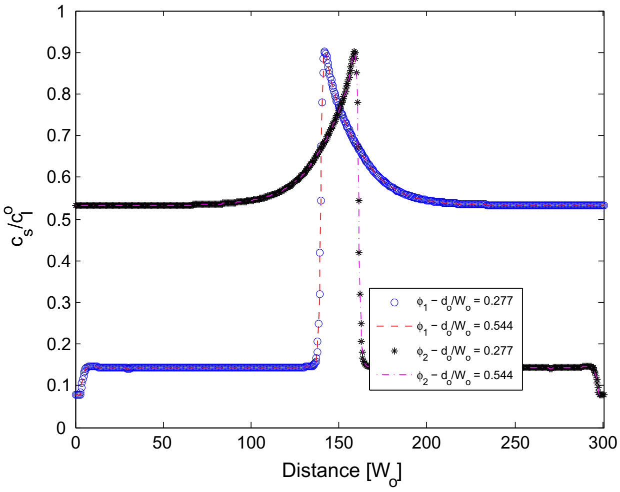

Fig. 2. Segregation profiles of the misoriented grains at time $1280\tau_o$, measured along the dendrite axis.

simulations it was found that for a large enough range of ω, there is always a range of undercooling, where $\phi_i + \phi_j \approx 1 - \delta\phi$ and $c_{max} \approx c_\infty + \delta c$, where $\delta\phi$ and δc are small. In this case, the steady-state concentration across a grain boundary is well approximated by:

$$c_o(\vec{\phi}_o) \approx \frac{c_\infty}{k}[1 - (1-k)h(\vec{\phi}_o)] \tag{38}$$

It will be seen in the next section (Fig. 3) that Eq. (38) actually holds very well for a range of temperatures below the solidus and interaction parameters ω.

5.2. Illustrating the balancing force of back-diffusion

Below the solidus temperature, any two phase fields ϕ_i and ϕ_j describing grains i and j will exhibit partial overlap in any multi-phase field model. In this model, the degree of overlap is set by the interaction parameter ω, which, in effect balances the force of back-diffusion driving ϕ_i and ϕ_j past each other. The overlap also implicitly determines the steady-state grain boundary concentration profile $c_o(\vec{\phi}_o)$ via Eq. (38).

To illustrate this balance, consider the steady-state driving force $\partial f_c/\partial\phi_i$ in Eq. (25) (with Eq. (27)) for a temperature below the solidus. Substituting Eq. (38) gives:

$$\begin{aligned}\frac{1}{H}\frac{\partial f_c(\vec{\phi}_o, c_o, T)}{\partial\phi_i^o} &= \bar{\lambda}\left(e^u - 1 - \frac{T - T_L}{m_L c_\infty}\right)\tilde{g}'(\phi_i^o)\\ &= \bar{\lambda}\frac{1}{k}\left(1 - k - \frac{T - T_L}{m_L(c_\infty/k)}\right)\tilde{g}'(\phi_i^o)\\ &= \bar{\lambda}\frac{\delta T}{m_L c_\infty}\tilde{g}'(\phi_i^o)\end{aligned} \tag{39}$$

where $\bar{\lambda} = \lambda/(1-k), \delta T = T_s - T$ and T_s is the solidus temperature. Substituting Eq. (39) into a steady-state version of Eq. (35) written for a planar interface gives:

$$\omega\int_{-\infty}^{\infty}\phi_i^o\left(\phi_j^o\right)^2\frac{d\phi_i^o}{dx}dx = \frac{\lambda\,\delta T}{m_L c_\infty(1-k)} \tag{40}$$

For the range of ω, where $\phi_i^o + \phi_j^o \approx 1$:

$$I = \frac{\lambda}{m_L c_\infty(1-k)}\frac{\delta T}{\omega} \tag{41}$$

where $I \approx \int_1^0 \phi_i^o(1-\phi_i^o)^2 d\phi_i^o \approx -1/12$. Eq. (41) illustrates how back-diffusion below the solidus is balanced by the interaction of phase fields, encapsulated by the overlap integral. Clearly as ω (which leads to a repulsive grain boundary interaction) increases, a higher undercooling is required to achieve the same degree of overlap.

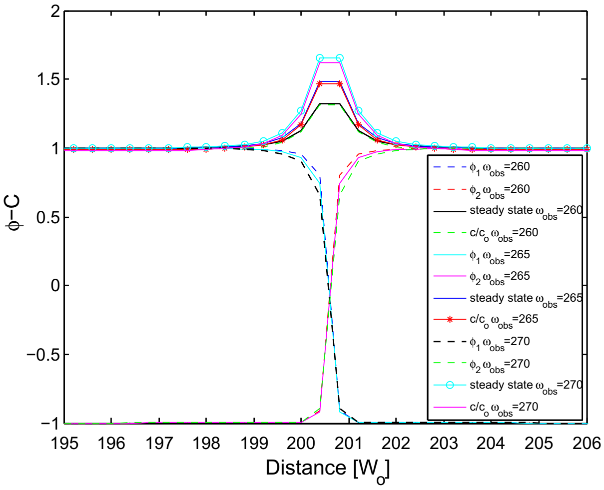

Fig. 3. Equilibrium concentration profiles of phase field and concentration for different values of the interaction parameter coefficient ω at an undercooling 220 K below the liquidus. The ratio of solid/liquid diffusion constants is $\xi = 10^{-2}$.

5.3. Coalescence

One-dimensional simulations of Eqs. (35) and (36) were conducted to examine the solidification and grain boundary coalescence of two adjacent grains. Phase field and process parameters used are listed in Table 2. Solidifying grains were cooled at a rate $\dot{q}$ to a temperature $\Delta T = 220$ K below the liquidus. Following solidification, back-diffusion occurred and eventually equilibrium was reached. During solidification, zero interface kinetics was assumed. For convenience, simulations were conducted using modified interpolation functions that allowed phase fields to vary from $-1 < \phi_i < 1$ than that from $0 < \phi_i < 1$.

Fig. 3 shows the numerical steady-state phase field and concentration profiles that are achieved for different ω. The corresponding steady-state profiles of Eq. (38) are within about 4% of the numerically evaluated ones. The range of ω selected allowed a wide range of undercoolings to be achieved without destabilizing the numerical solutions. It is emphasized that grain boundary merger becomes possible because of the thermodynamic driving force that develops as a result of back-diffusion. The grain boundary segregation evidenced in Fig. 3 is an example of grain boundary adsorption. The degree of solute segregation at the grain boundary depends on ω as well as W_o, and is a property inherent in all phase field models as shown by McFadden and Wheeler [34].

Table 2
Simulation and alloy parameters used for grain boundary coalescence simulations. L_f is the latent heat of fusion and $\dot{q}$ is the cooling rate and c_∞ is the average alloy concentration.

Parameter	Value
W_o	1
λ	7
Δx	0.4 (W_o)
Δt	0.008 (τ_o)
D_L	1×10^{-10} m^2/s
$\dot{q}$	−5 K/s
L_f	1×10^9 J/m^3
T_m	1000 K
m_L	−500 K
k	0.15
c_∞	0.05

To model orientational dependence of grain boundary energy when two order parameters overlap, the form of W and τ interpolate to a form that produces the correct general physical behavior required of solid–solid systems. Specifically $W(\vec{\phi})$ follows the Read–Shockley form:

$$W(\vec{\phi}) = W_o\theta\{1 - \ln(\theta/\theta_m)\}\{1 + \epsilon_4\cos(4\psi)\} \tag{42}$$

where W_o sets the isotropic interfacial energy, θ is the local misorientation angle between grains i, j and θ_m is the misorientation for which a grain boundary energy reaches its maximum. The angle ψ is the local orientation of a grain boundary with respect to an external reference axis. The local misorientation angle θ between grain i and j is given by: $\theta(\mathbf{r}) = \sum_{ij}^{N}\phi_i^2\phi_j^2\vartheta_{ij}/\sum_{ij}^{N}\phi_i^2\phi_j^2$, where ϑ_{ij} is the global misorientation of grains i, j [35]. Prior to establishing the misorientation angle, the denominators are first evaluated to establish interaction between grains. The choice is also made to have the time constant (inverse mobility) $\tau(\vec{\phi})$ take on a similar form as that of the gradient term, i.e. to lowest order:

$$\tau(\vec{\phi}) = [\tau_o\theta\{1 - \ln(\theta/\theta_m)\}\{1 + \epsilon_4\cos(4\psi)\}]^{-1} \tag{43}$$

5.4. Solid–solid interface energy

Surface energy is defined as the excess of the grand potential through a planar interface. Namely:

$$\gamma = \int_{-\infty}^{\infty}\left[\Phi^G(\vec{\phi}_o, c_o) - \Phi_E^G\right]dx \tag{44}$$

where $\Phi^G(\vec{\phi}_o, c_o) = f(\vec{\phi}_o, c_o) - \mu_{\mathrm{E}}c_o(\vec{\phi}_o(x))$ and where $\Phi_E^G = f(\vec{\phi}_o = \hat{e}_i, c_s) - \mu_{\mathrm{E}}c_s$. Here, $f(\vec{\phi}, c)$ represents all terms in the free energy density of Eq. (2), μ_{E} is the equilibrium chemical potential, c_s is the bulk solid reference concentration and $c_o(\vec{\phi})$ is the steady-state concentration through the interface, which depends only on the phase fields $\{\phi_i\}$, as shown in Section 2.3. For the range of interaction parameters ω and undercooling studied here, $\phi_i + \phi_j$ is quite close to unity in the grain boundary. In this limit it is straightforward to show, using Eq. (39), that:

$$\gamma \approx \int_{-\infty}^{\infty}\left[\frac{W_o^2}{2}\sum_i\left(\frac{d\phi_i^o}{dx}\right)^2 + \sum_i f_{\mathrm{D}}(\phi_i^o)\right.$$
$$\left. + \,\omega\sum_i\sum_{j\neq i}(\phi_i^o)^2(\phi_j^o)^2 - f_D(\hat{e}_i)\right]dx \tag{45}$$

The coefficients W_o and ω can be tuned to produce a range of surface energies. For the case of a single grain, Eq. (45) reduces to Eq. (14). For wet grain boundaries the surface energy is thus $2\gamma_{sl}$.

To quantify grain boundary energy vs. misorientation, two grains were slowly cooled to a temperature T below the solidus. Solidification, back-diffusion and coalescence were allowed to occur, and the subsequent surface energy calculated for different misorientations. The parameters used in these simulations are listed in Table 2 with $\xi = 10^{-2}$. Fig. 4 shows the grain boundary energy vs. misorientation for several values of undercooling below the solidus. Here the undercooling was chosen for each interaction parameter ω such as to satisfy Eq. (41). Each individual curve follows the Read–Shockley behavior. The small high-angle variation is due to the use of Eq. (41), which maintains approximately a constant interaction energy for all undercoolings in the range examined.

Variation of high-angle grain boundary energies can be achieved by changing the gradient energy coefficient W_o. This is seen in Fig. 5, which simulates grain boundary energy vs. misorientation for two W_o. The simulations were both done at the same undercooling below the solidus and for the same grain interaction term ω. For the bottom curve, $W_o = 1$ in Eq. (42) and in the top curve $W_o = 2$. The change in energy due to W_o is a volume effect as W_o sets the the volume (area in two dimensions) of undercooled grain boundary material. Through a combination of different gradient energy coefficients W_o and interaction parameters ω, it is thus possible to emulate a range of grain boundaries energies, once these are in principle known from experiments.

5.5. Solidification path and back-diffusion

The solidification path during back-diffusion and grain boundary merger was also characterized for the case of slow continuous cooling below the solidus. Fig. 6 shows the average concentration of the solid and liquid in the grain boundary, each superimposed, respectively, on the phase diagram during cooling. The parameters used for these simulations are listed in Table 2. The interaction parameter here was fixed $\omega = 270$. Solidification paths for three ratios of solid/liquid diffusion coefficients ξ are shown.

Fig. 6 shows that the liquidus line is followed quite faithfully by the average liquid concentration, until the

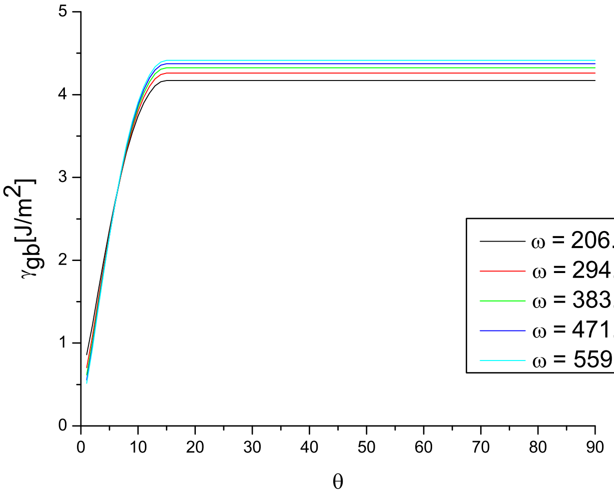

Fig. 4. Grain boundary energy as a function of misorientation for several final quench temperatures. For each interaction parameter, the undercooling was chosen to satisfy Eq. (41).

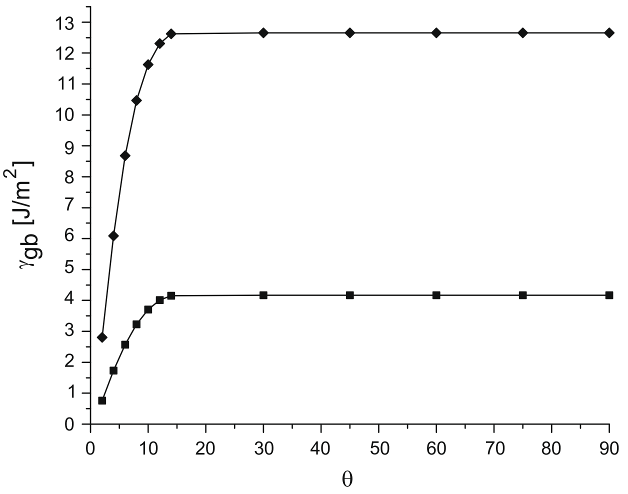

Fig. 5. Grain boundary energy for a given temperature 200 K below the initial liquidus and $\omega = 270$ for different values of W_o. The curve represented by the square symbols is for the $W_o = 1$ path and the other for $W_o = 2$.

interfaces approach and start interacting. At this point the fraction of solid is approximately equal to 1 and what remains is a thin supersaturated liquid film, effectively requiring an unrealistically large undercooling for coalescence without the aid of back-diffusion. It is also noted that while the solid fraction increases monotonically with decreasing temperature, the average solid concentration quickly approaches the average value of the alloy. Before the deviation of the average liquid concentration from the liquidus line, when the system is still undergoing cooling, little solute is rejected into the already supersaturated thin film of liquid. Activating back-diffusion, however, causes the average concentration in the interdendritic space to decrease and cross the two-phase region of the phase diagram, for all three diffusion constants.

These results are consistent with the work of Rappaz et al. [29]. It can be seen in Fig. 6 that the smaller the solid diffusion, the lower the undercooling required and the longer the simulation time before the effects of back-diffusion are realized, thus closing the grain boundary. It should be noted that the average solid is relatively uninfluenced by this late-stage solidification process as the thin film of liquid represents a very small volume fraction. The behavior of the data in Fig. 6 also agrees qualitatively with the sharp interface and multi-phase field results reported in Ref. [29]. The differences in the appearance of the plots, specifically with the sharp-interface results, can be attributed to the diffusiveness of the interface. At coalescence the diffusiveness of the interface enhances diffusion along the interface. This is seen in Fig. 6, where the deviation of the average liquid concentration from the liquidus commences slightly earlier. Note that the curve for the fastest back-diffusion coefficient does not seem to suffer from this to a noticeable degree. A way to reduce this effect may be to dynamically thin the interface at the onset of coalescence as done in Ref. [13]. In general, however, this deviation from the liquidus line is minor.

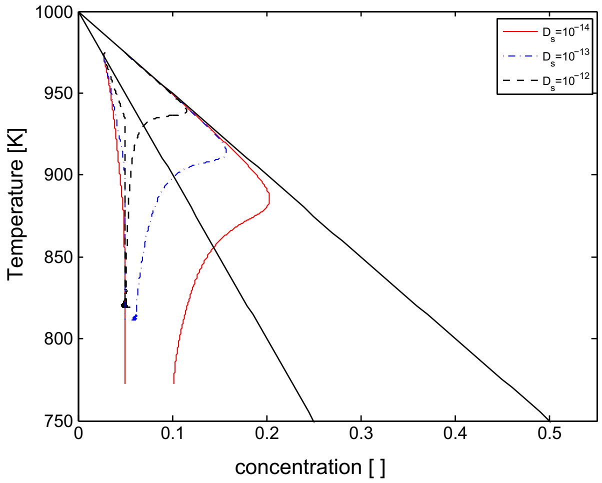

Fig. 6. Effect of back-diffusion on solidification path and coalescence for different solid diffusion constants.

6. Two-dimensional simulations of late stage solidification

Fig. 7 shows a two-dimensional simulation of the solidification and coalescence of four randomly oriented grains

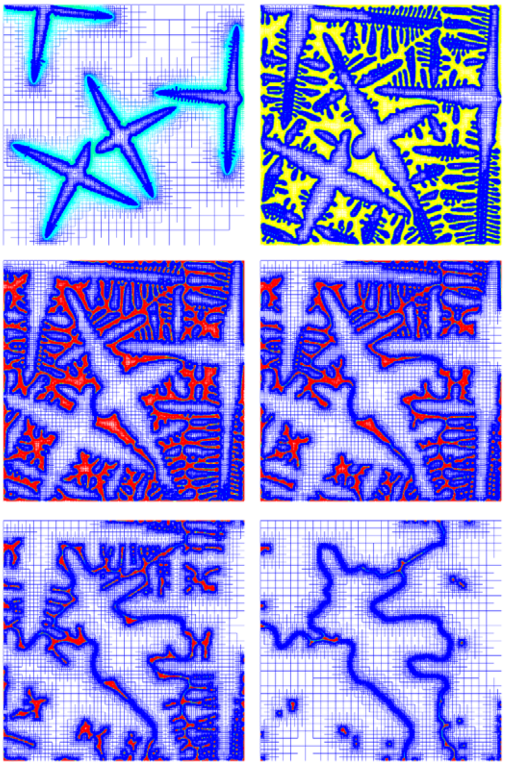

Fig. 7. Microstructural evolution of four crystals, where gray scale represents concentration (in black and white). In color, low concentration values are seen as lighter shades (colder colors), while the darker shades (warmer colors) represent higher concentrations. From top left to bottom right, corresponding times are $1600\tau_o$, $3200\tau_o$, $4800\tau_o$, $6400\tau_o$, $8000\tau_o$ and $11,200\tau_o$, respectively.)

corresponding to the parameters listed in Table 2. The system was cooled to a temperature 60 K below the solidus. The microstructure for several times is shown. The gray scale corresponds to concentration, with dark shades corresponding to a high concentration and lighter shades to lower. (Online, warmer colors represent higher concentration and cooler colors lower concentration.)

The images in Fig. 7 model the microstructure and segregation from the free dendritic growth stage at early times, the emergence, growth and interaction of secondary dendrite arms at intermediate times, to the onset of coalescence and coarsening at late times, respectively. In a follow-up publication, the model developed in this work, will be used to statistically correlate secondary arm spacing and solute segregation trends in equiaxed solidification during late stage solidification of aluminum alloys.

7. Conclusions

A new multi-order parameter phase field model has been developed for binary alloy solidification. The quantitative behavior during free dendrite growth has been demonstrated for multiple grains, showing good convergence with different interface widths. The model was shown to yield the correct physics of back-diffusion during grain coalescence, and was able to model a range of grain boundary energies and interface segregation profiles. As with all multi-phase field models, grain boundary energy is treated here phenomenologically. A more detailed understanding of grain boundary structure, segregation and energies requires further research using more fundamental approaches such as phase field crystal modeling, wherein the interplay of thermodynamics and atomic scale grain boundaries can be simultaneously modeled in alloys. This will be studied in future work.

Acknowledgments

We would like to thank the National Science and Engineering Research Council of Canada (NSERC), Novelis Inc and the McMaster Steel Research Centre (SRC) for financial support of this work.

References

[1] Caginalp G. Anal Phys 1986;172:136.
[2] Caginalp G, Socolovsky E. SIAM J Sci Comput 1991;15:106.
[3] Karma A. Phys Rev Lett 2001;87:115701.
[4] Kim SG, Kim WT, Suzuki T. Phys Rev E 1999;60:7186.
[5] Chen LQ. Annu Rev Mater Sci 2002;32:113.
[6] Zhu J, Wang T, Zhou S, Lui Z, Chen L. Acta Mater 2004;52:833.
[7] Echebarria B, Folch R, Karma A, Plapp M. Phys Rev E 2004;70:061604.
[8] Folch R, Plapp M. Phys Rev E 2005;72:011602.
[9] Bottger B, Eiken J, Steinbach I. Acta Mater 2006;54:2697.
[10] Mecozzi M, Sietsma J, Zwaag SVD, Apel M, Schaffnit P, Steinbach I. Metall Mater Trans A 2005;36:2327.
[11] Kim SG. Acta Mater 2007;55:4391.
[12] Almgren R. SIAM J Appl Math 1999;59:2086.
[13] Tong C, Greenwood M, Provatas N. Phys Rev E 2008;77:1.
[14] Karma A, Rappel W-J. Phys Rev E 1996;53:R3017.
[15] Provatas N, Goldenfeld N, Dantzig J. Phys Rev Lett 1998;80:3308.
[16] Provatas N, Dantzig J, Goldenfeld N. J Comput Phys 1999;148:265.
[17] Athreya BP, Goldenfeld N, Dantzig JA, Greenwood M, Provatas N. Phys Rev E 2007;76:056706.
[18] Provatas N, Wang Q, Haataja M, Grant M. Phys Rev Lett 2003;91.
[19] Greenwood M, Haataja M, Provatas N. Phys Rev Lett 2004;93:246101.
[20] Daniov D, Nestler B. Phys Rev Lett 2004;93:215501.
[21] Nestler HGB, Stinner B. Phys Rev E 2005;71:041609.
[22] Kazaryan A, Wang Y, Dregia SA, Patton BR. Acta Mater 2002;50:2491.
[23] Moelans N, Blanpain B, Wollants P. Acta Mater 2006;54:1175.
[24] Nestler B, Wendler F, Selzer M, Stinner B, Garcke H. Phys Rev E 2008;78:011604.
[25] Moelans N, Blanpain B, Wollants P. Phys Rev Lett 2008;101:025502.
[26] Garcke H, Nestler B, Stoth B. SIAM J Appl Math 1999;60:295.
[27] Steinbach I. Model Simul Mater Sci Eng 2009;7:073001.
[28] Ofori-Opoku N. MASc thesis, McMaster University; 2009.
[29] Rappaz M, Jacot A, Boettinger WJ. Metall Mater Trans A 2003;34A:467.
[30] Zhu J, Wang T, Ardell A, Zhou S, Lui Z, Chen L. Acta Mater 2004;52:2837.
[31] Kazaryan A, Wang Y, Dregia SA, Patton BR. Phys Rev B 2001;63:184102.
[32] Zhu JZ, Wang T, Ardell AJ, Zhou SH, Liu ZK, Chen LQ. Acta Mater 2004;52:2837.
[33] Warren JA, Kobayashi R, Lobkovsky AE, Carter WC. Acta Mater 2003;51:6035.
[34] McFadden GB, Wheeler AA. Proc Roy Soc Lond A 2002;258:1129.
[35] Ma N, Kazaryan A, Dregia SA, Wang Y. Acta Mater 2004;52:3869.